Supporting Information

Discharge-Triggered Electronic Delocalization via Asymmetric Motifs Suppresses Jahn-Teller Distortion in Mn-Based Layered Oxides

Jiayuan Zhang,[a,#] Yucheng Fu,[b,#] Xingyu Lu,[d,#] Longxiang Liu,[c] Tianwei Cui,[a] Hong Zhu,[b] Yongzhu Fu[a,*] and Xiang Li[a,*]

Material Synthesis

$Na_{0.69}Li_{0.23}Ru_{0.17}Mn_{0.6}O_2$ and $Na_{0.69}Li_{0.23}Mn_{0.77}O_2$ were synthesized by traditional solid-state methods. Stoichiometric amounts of Na_2CO_3 (3% excess), Li_2CO_3 (3% excess), RuO_2, and MnO_2 were thoroughly mixed and ground for half an hour with a mortar and pestle. Then the mixed powder was pelleted and calcined at 800 ℃ in air for 12 h, then cooled to room temperature naturally and transferred into a glove box for further electrode preparation.

Electrochemical Measurements

2032 coin-type cells were used for electrochemical measurements. Electrodes were consisted of active material, Super P, and polytetrafluoroethene (PTFE, 12 wt.%) binder with the weight ratio of 7:2:1. 1 M $NaClO_4$ in ethylene carbonate (EC) and propylene carbonate (PC) (1:1 in volume) with 5% fluoroethylene carbonate (FEC) was used as the electrolyte, and the glass fiber film was employed as a separator. The galvanostatic charge/discharge tests were performed by using a Land battery testing system (Wuhan, China) at different conditions. Charge and discharge measurements were performed in a voltage range of 2–4.3 V at 25 °C (for some special tests, the voltage range is 1.5–4.5 V). The relaxation procedure after charge was tested by a rest step until the voltage tended to be stable. The relaxation procedure after discharge was tested by a constant voltage discharge process at 2.2 V until the current reached 1/20th of the initial current. The relaxation test is performed using the Bio-Logic electrochemical workstation (French). Both electrodes were brought to the same initial state (galvanostatic discharge to 2.0 V) before the relaxation measurement. For the *ex-situ* characterizations, the electrodes were collected by disassembling the electrochemical cells inside an Ar-filled glovebox and then washed three times with dimethyl ether (DME).

Structural Characterizations

The XRD patterns of $Na_{0.69}Li_{0.23}Ru_{0.17}Mn_{0.6}O_2$ were identified by a Rigaku SmartLabSE X-ray diffractometer (Cu source, λ= 1.54056 Å) in the 2θ range of 10°−80°. In situ XRD patterns were tested from 10°−50° with a speed of 2° per min. The morphology of the powder was characterized by a field emission scanning electron microscope (FE-SEM, Carl Zeiss Sigma 500). HAADF-STEM images were collected at different cycled states and performed at Themis Z (3.2) at Thermo Scientific with Focused Ion Beam (FIB) cut technology. XPS was characterized by using Thermo Scientific K-Alpha. Mn and Ru K-edge XAS spectra were collected at the Shanghai Synchrotron Radiation Facility (SSRF) in Shanghai, China. The O K-edge soft XAS measurements were conducted at the Hefei Synchrotron Radiation Laboratory (HLS).

^{7}Li Magic Angle Spinning (MAS) NMR experiments were performed on a Bruker-AVANCE-500M NMR spectrometer (11.74 T) with the ^{7}Li Larmor frequency of 194.3 MHz using a 1.3 mm double-resonance MAS probe. The samples were packed into 1.3 mm MAS rotors in an argon-filled glove box, and the sample spinning rate of 55 kHz was used during the measurements. The pjMATPASS experiment was used to eliminate the sidebands with π /2 pulse width of 1.5 μs and a recycle delay of 0.1 s; 1 M LiCl with the chemical shift at 0 ppm was employed as the reference.

Differential electrochemical mass spectrometry (DEMS) measurements were carried out using a homemade cell connected to the equipment from Perkin-Elmer (Clarus 680 and SQ 8S). The charge/discharge mode is set as follows: first, the cell was charged at a constant current to 4.4 V, then maintained at a constant voltage for one hour, followed by a discharging process at a constant current. A total of one and a half cycles of testing are performed.

Density functional calculation

Spin-polarized density functional theory (DFT) calculations were performed using Vienna Ab initio Simulation Package. The generalized gradient approximation (GGA) with the Perdew-BurkeErnzerhof functionals was used to describe the exchangecorrelation potentials. Also, the projector-augmented wave method was used. For a correction of self-interaction error in the d orbital states of TM ion, the Hubbard U correlations were adopted (U = 4.0 (ref. 1) and 4.88 (ref. 2) for Mn and Ru, respectively). All DFT calculations used a plane wave basis set with an energy cutoff of 520 eV. The atomic position, cell shape, and volume of the structures are fully relaxed (ISIF = 3) until the residual forces on the cell are smaller than 0.02 $eV \cdot Å^{-1}$ for all cases. Antiferromagnetic initial setting was applied to all structures after comparing its energy to ferromagnetic results. The method to prepare the structures and further computational details are provided in the following. The isosurface in Fig.6e and 6f is prepared by clipping electron density around 1.3 Å of selected atoms and the threshold for electron density is 0.1 $e/Bohr^3$.

Method for computational modeling: To compare the computational results between pristine and discharged state of doped and undoped structure, we designed its structural modeling as follows. A cell size is minimized to evaluate a cost-expensive electronic structure. The size of supercell is 2 × 2 × 1, consisting of 18 Na, 6 Li, 4 Ru, 14 Mn and 48 O atoms for pristine NLRMO. The discharged state was determined by reducing 4 Na and 4 O. NLMO is the same supercell size with 18 Mn. For each composition, 100 structures were generated by pymatgen given the partial occupancy. Then a machine learning potential MatterSim is imploted for preliminary screening. The top 5 structures with the lowest energy was relaxed

and the lowest after relaxation is used for DFT relaxation and statistic calculation. Reciprocal space k-point meshes were 3 × 3 × 2 for all case. The crystal orbital Hamiltonian populations (COHP) method was applied using LOBSTER for molecular orbital analysis of the DOS features and the ICOHP for describing the bond energies of Mn-O and Ru-O bonding. For the modeling of the supercells at the end of discharge, we took the features of anionic redox into account (the loss of lattice oxygen) and removed 4 Na atoms and 4 O atoms relative to the pristine state, according to experimental composition.

Supplementary Figures

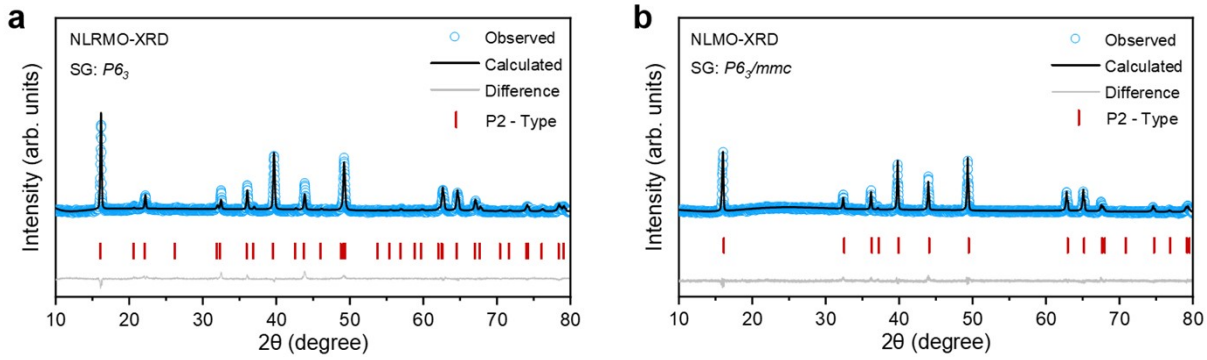

Fig. S1. XRD patterns and Rietveld refinements results of (a) NLRMO and (b) NLMO.

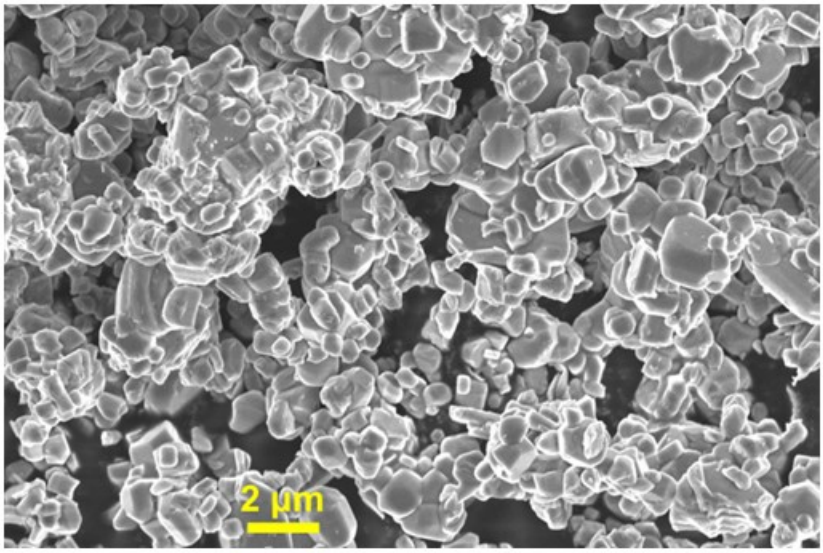

Fig. S2. SEM images of NLMO.

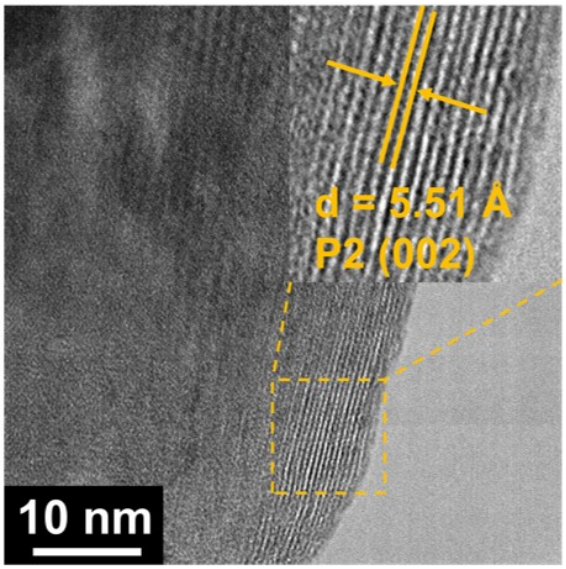

Fig. S3. TEM images of NLMO.

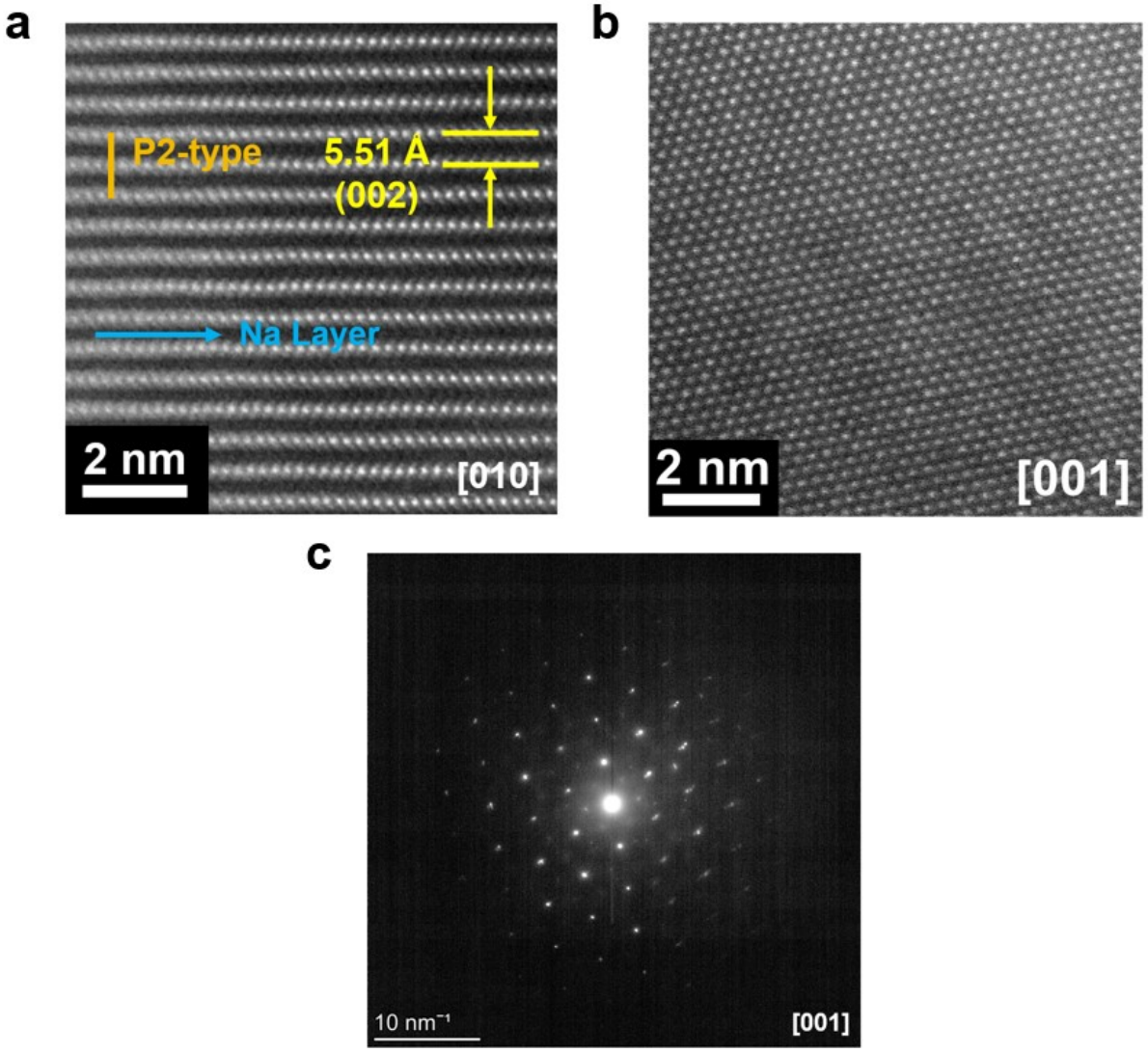

Fig. S4. HAADF-STEM images of NLMO (a) along the [010] zone axis and (b) along the [001] zone axis. (c) SAED pattern along the [001] zone axis.

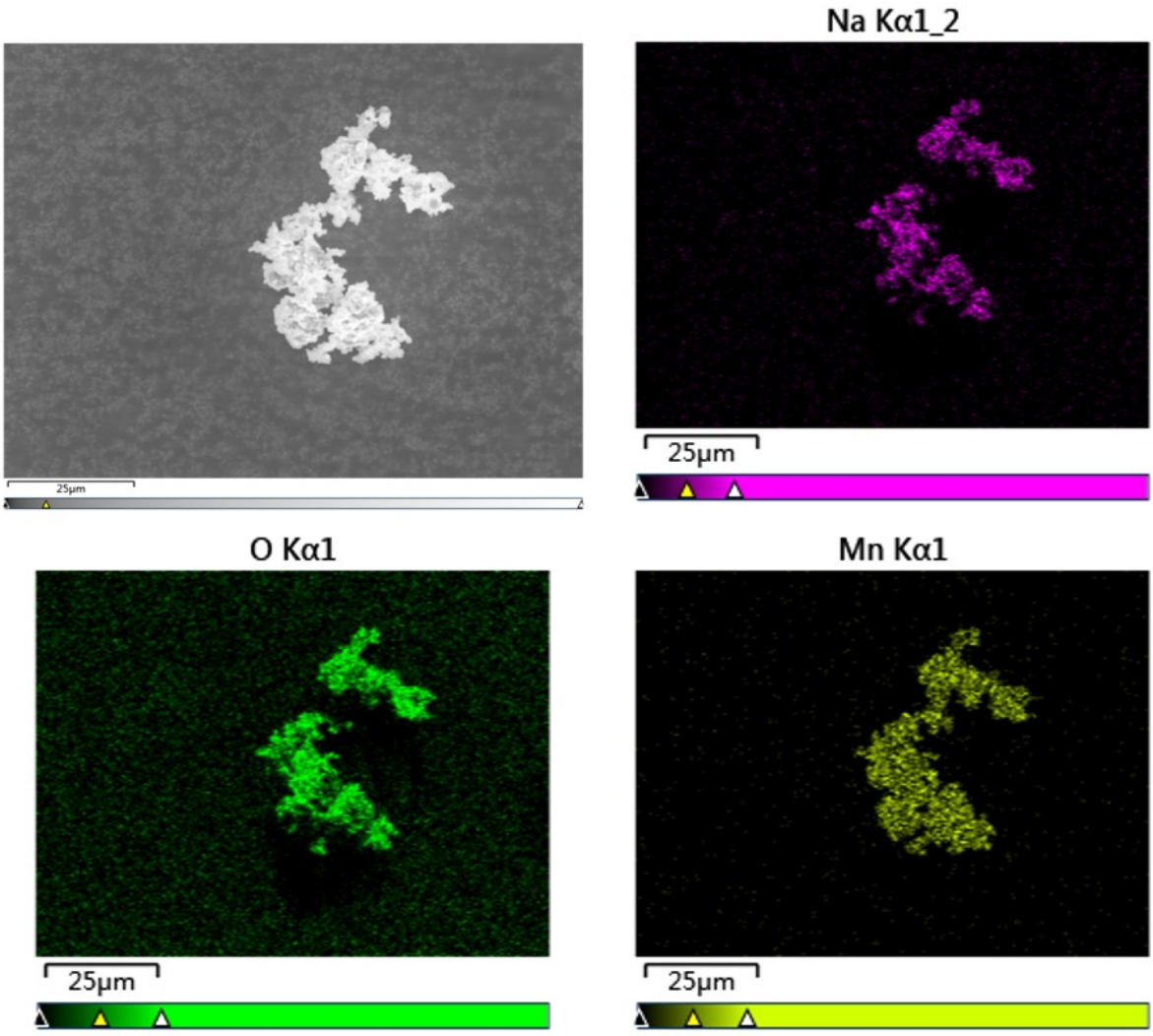

Fig. S5. SEM images and the corresponding EDS elemental mappings of NLMO.

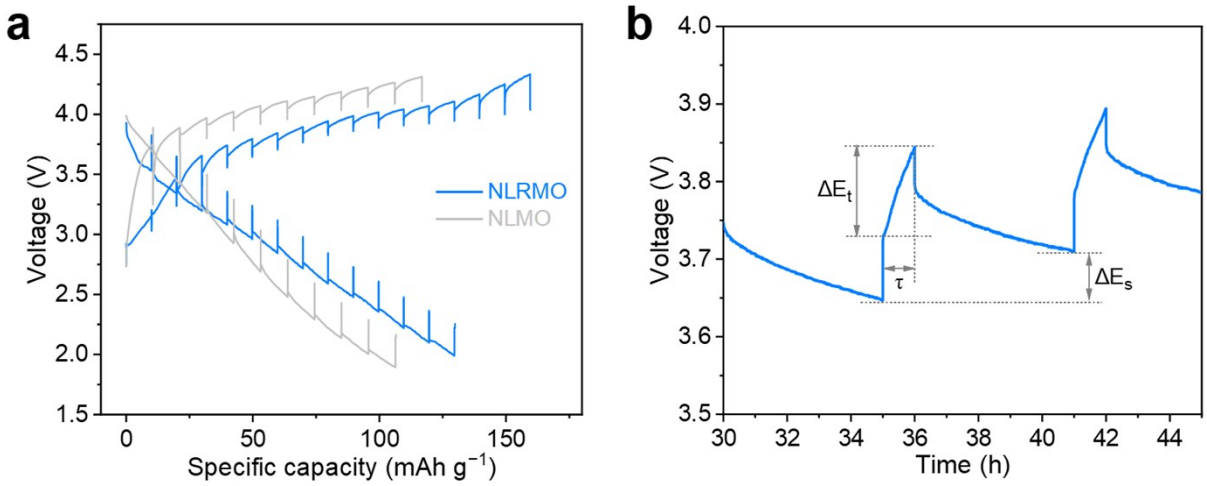

Fig. S6. (a) GITT curves of NLRMO and NLMO. (b) Selected steps from the GITT curves of NLRMO during charging process. The Na^+ diffusion coefficients can be determined by the following equation:

$$D_{Na+} = \frac{4}{\pi\tau}\left(\frac{n_m V_m}{S}\right)^2\left(\frac{\Delta E_s}{\Delta E_t}\right)^2$$

where τ is the pulse time, n_m and V_m stand for the molar number and molar volume of the active material, respectively. S represents the area of the electrode, ΔE_s is the change in the steady state potential and ΔE_t is the total change by subtracting IR drop. The cell was charged at 10 mA g^{-1} for 1 h, followed by relaxing for 5 h to reach voltage equilibrium.

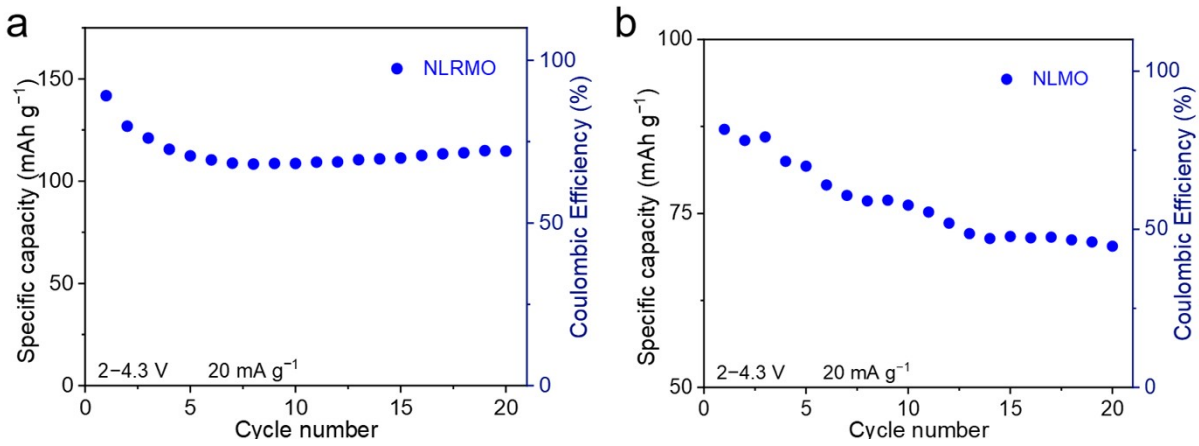

Fig. S7. Cyclic performance of (a) NLRMO and (b) NLMO at 20 mA g^{-1} between 2−4.3 V.

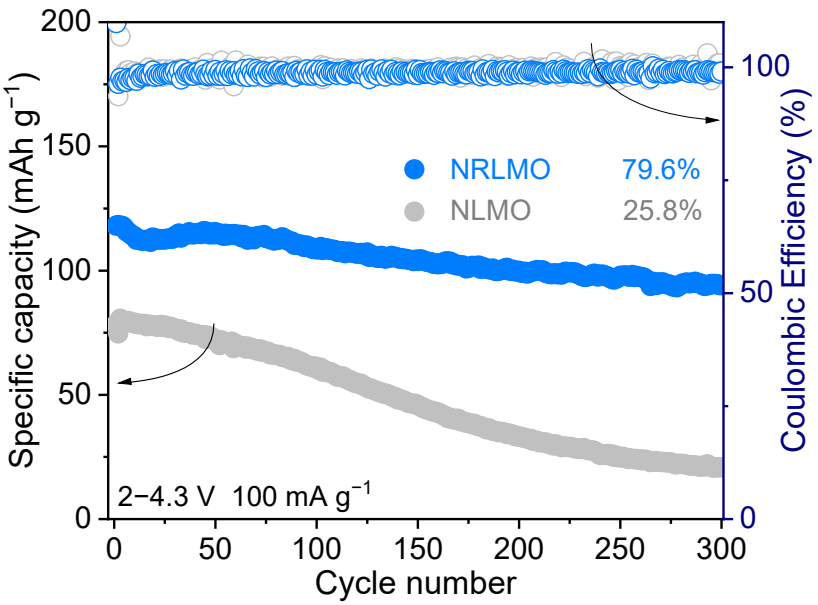

Fig. S8. Cyclic performance of NLRMO and NLMO at 100 mA g^{-1} between 2−4.3 V.

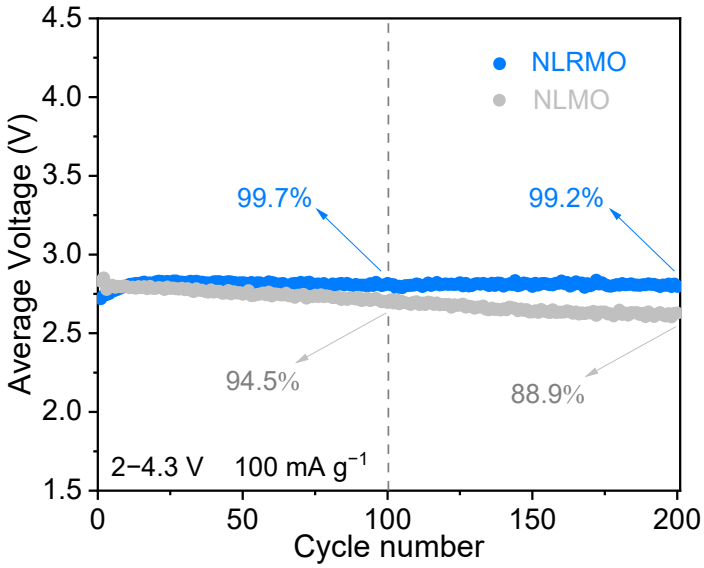

Fig. S9. The comparison of average voltage of NLRMO and NLMO for 200 cycles at 100 mA g^{-1}.

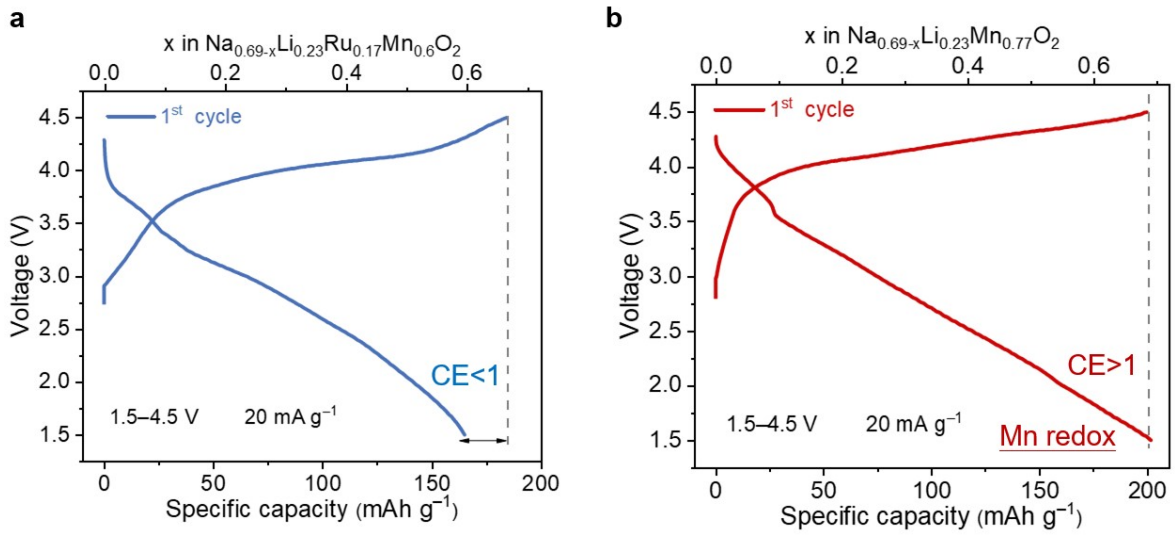

Fig. S10. Initial charge/discharge curves of (a) NLRMO and (b) NLMO at 20 mA g^{-1} between 1.5 and 4.5 V.

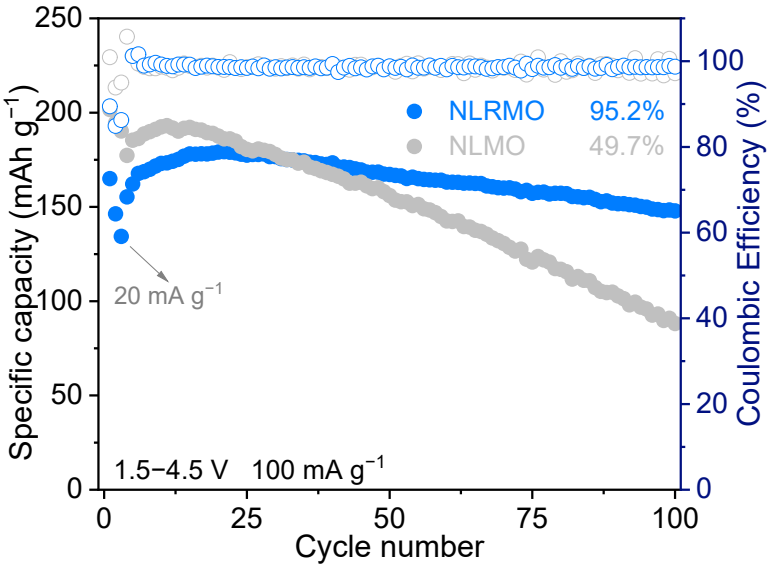

Fig. S11. Cyclic performance of NLRMO and NLMO at 100 mA g^{-1} between 1.5 and 4.5 V.

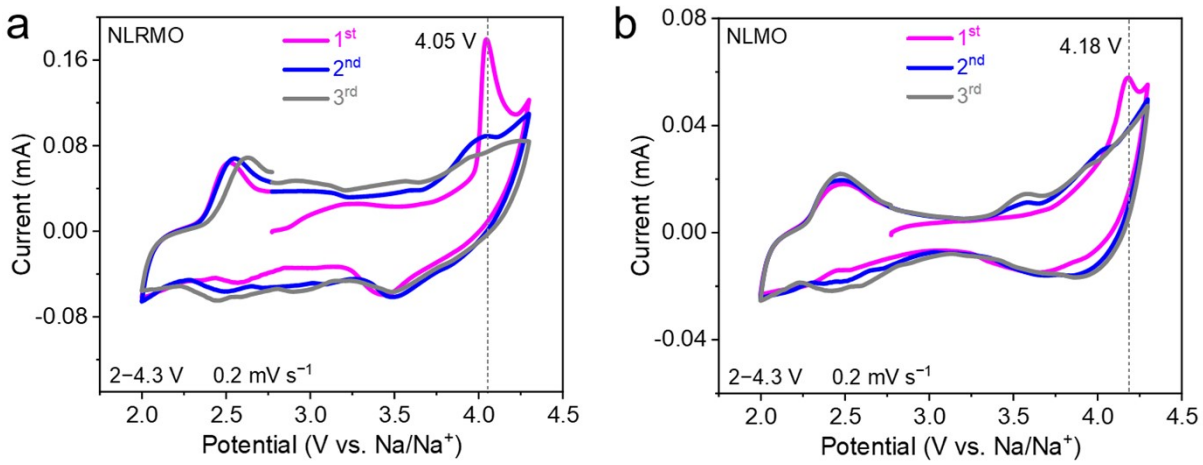

Fig. S12. Cyclic voltammetry curves of (a) NLRMO and (b) NLMO at a scan rate of 0.2 mV s^{-1} during the first three cycles.

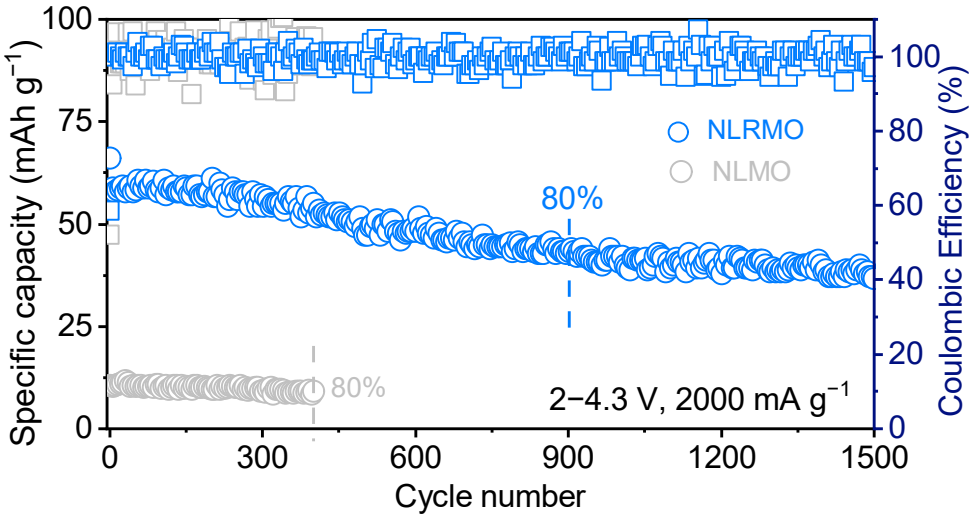

Fig. S13. Cyclic performance of NLRMO and NLMO at 2000 mA g^{-1} between 2 and 4.3 V.

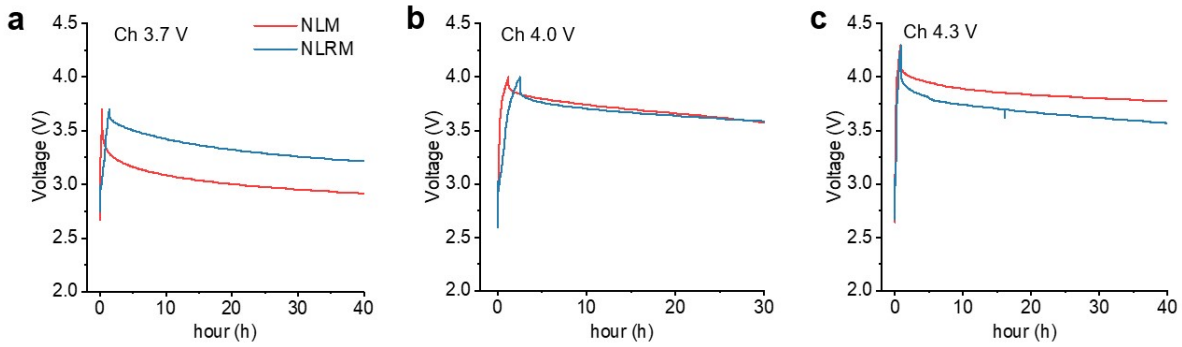

Fig. S14. Long-term relaxation processes for both cathodes at different cut-off voltages. (a) Electrode charged to 3.7 V with a subsequent rest time of 40 h. (b) Electrode charged to 4.0 V with a rest time of 30 h. (c) Electrode charged to 4.3 V with a rest time of 40 h.

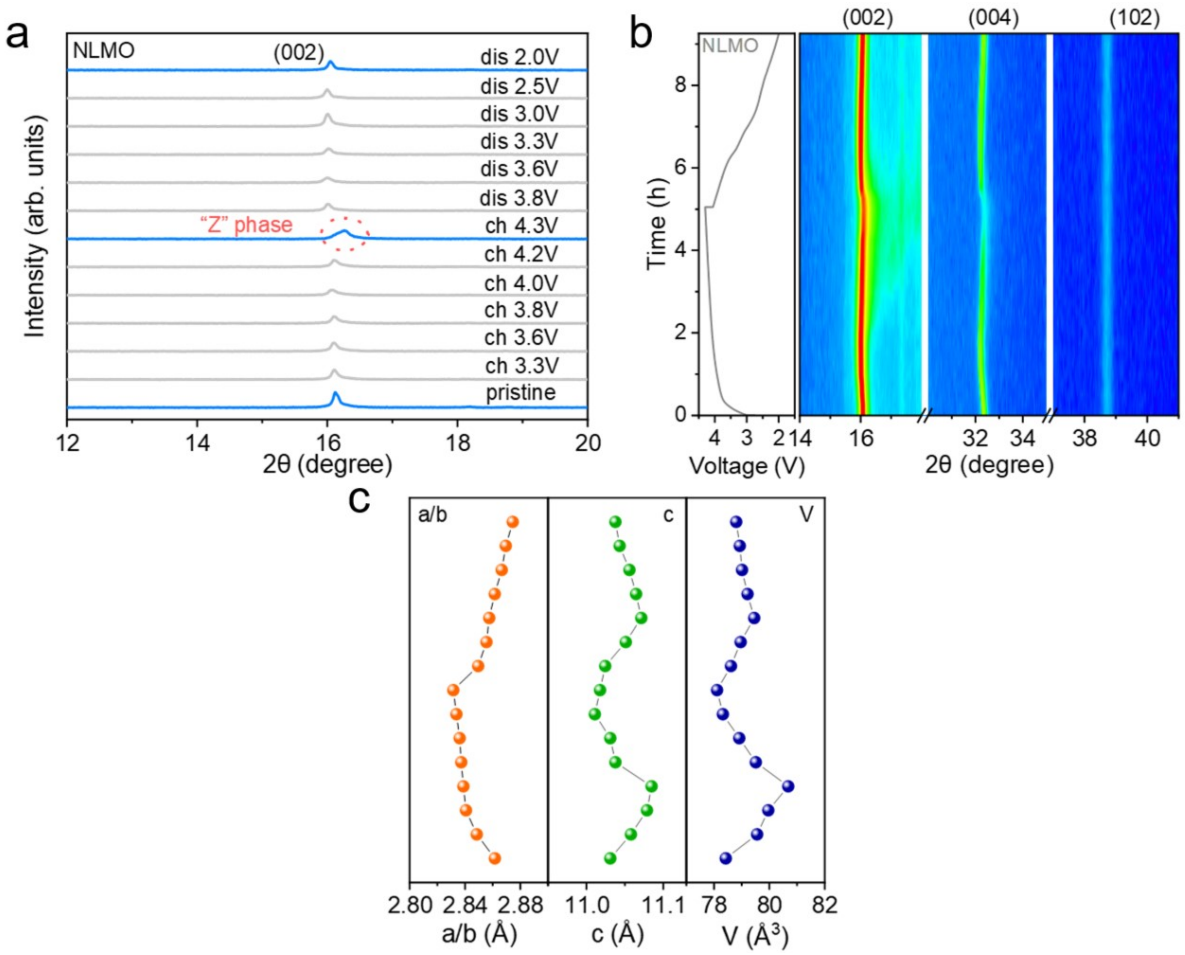

Fig. S15. (a) Ex situ and (b) in situ XRD patterns of NLMO. (c) The corresponding lattice parameter during the first charge/discharge cycle range.

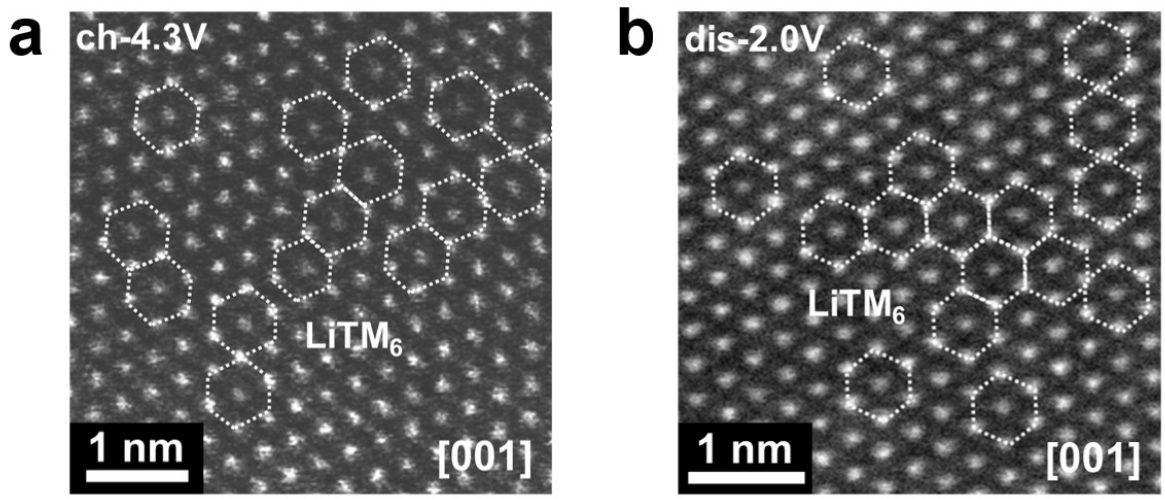

Fig. S16. HAADF-STEM image of NLRMO. (a) the 4.3 V-charged state and (b) the 2.0 V-discharged state along the [001] zone axis.

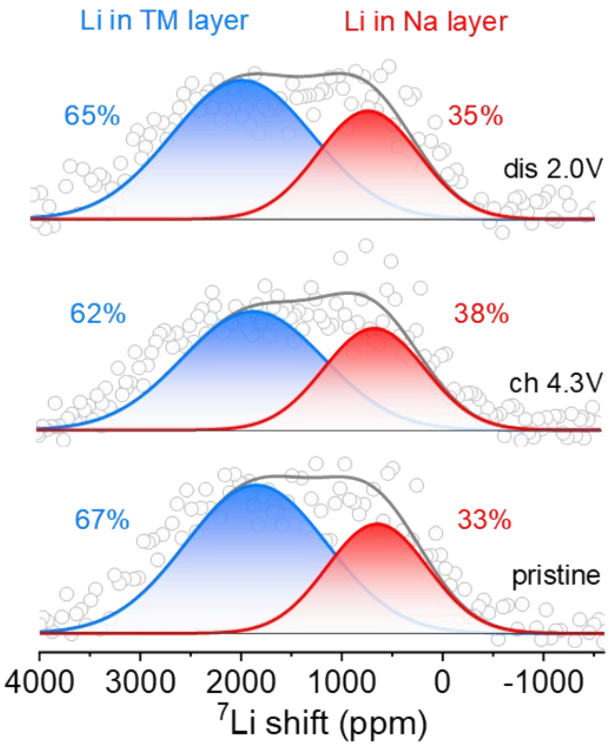

Fig. S17. ^{7}Li SS-NMR spectra of NLMO during the initial cycle.

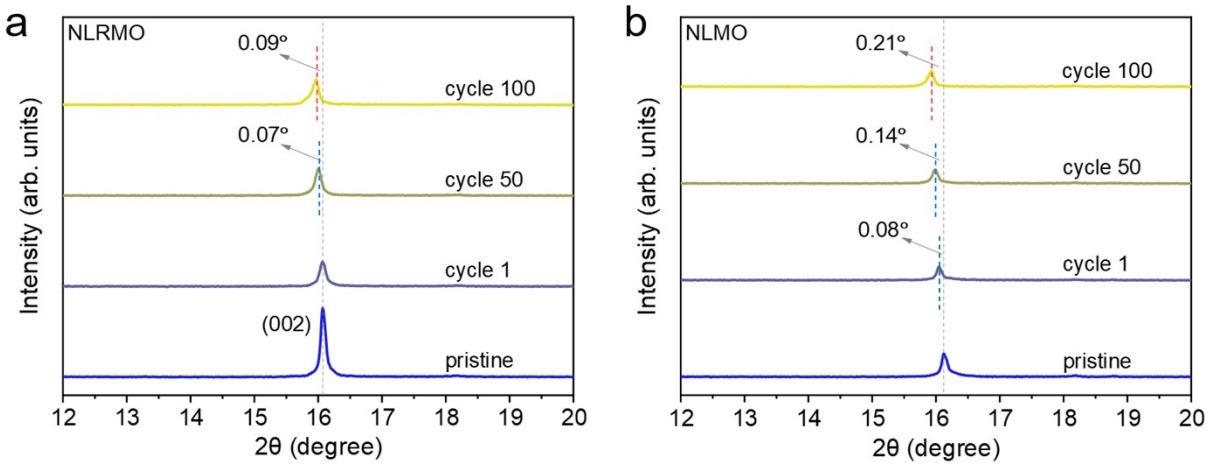

Fig. S18. Ex situ XRD of (a) NLRMO and (b) NLMO after 50 and 100 cycles.

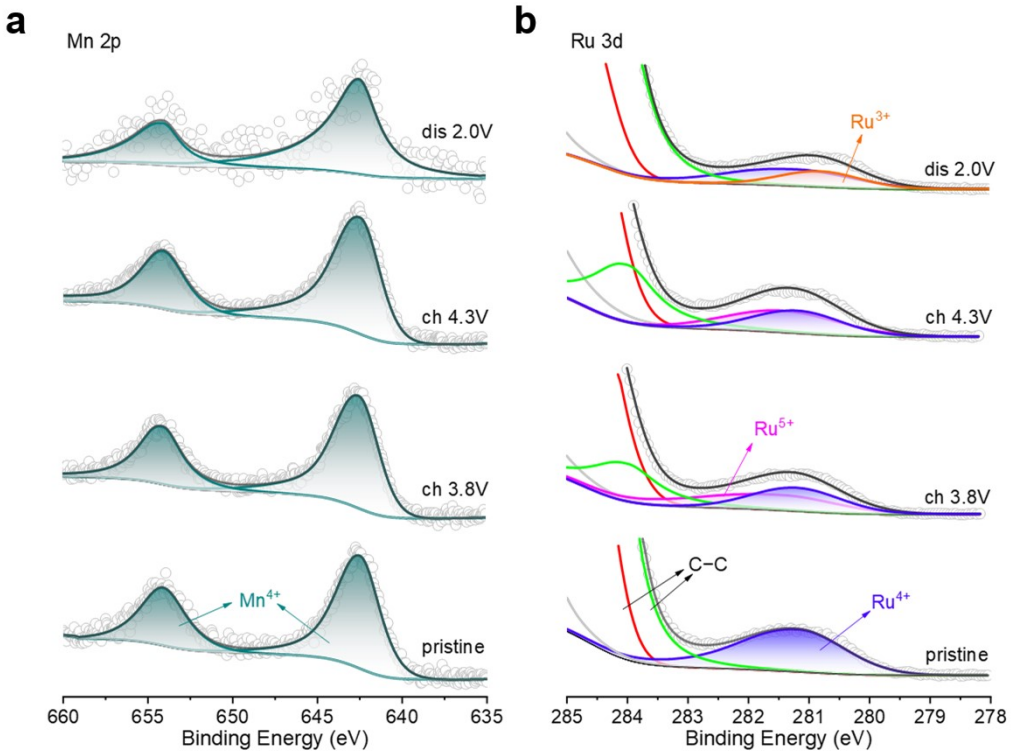

Fig. S19. Ex situ XPS analysis of NLRMO. XPS results of (a) Mn 2p, (b) Ru 3d during the initial cycle.

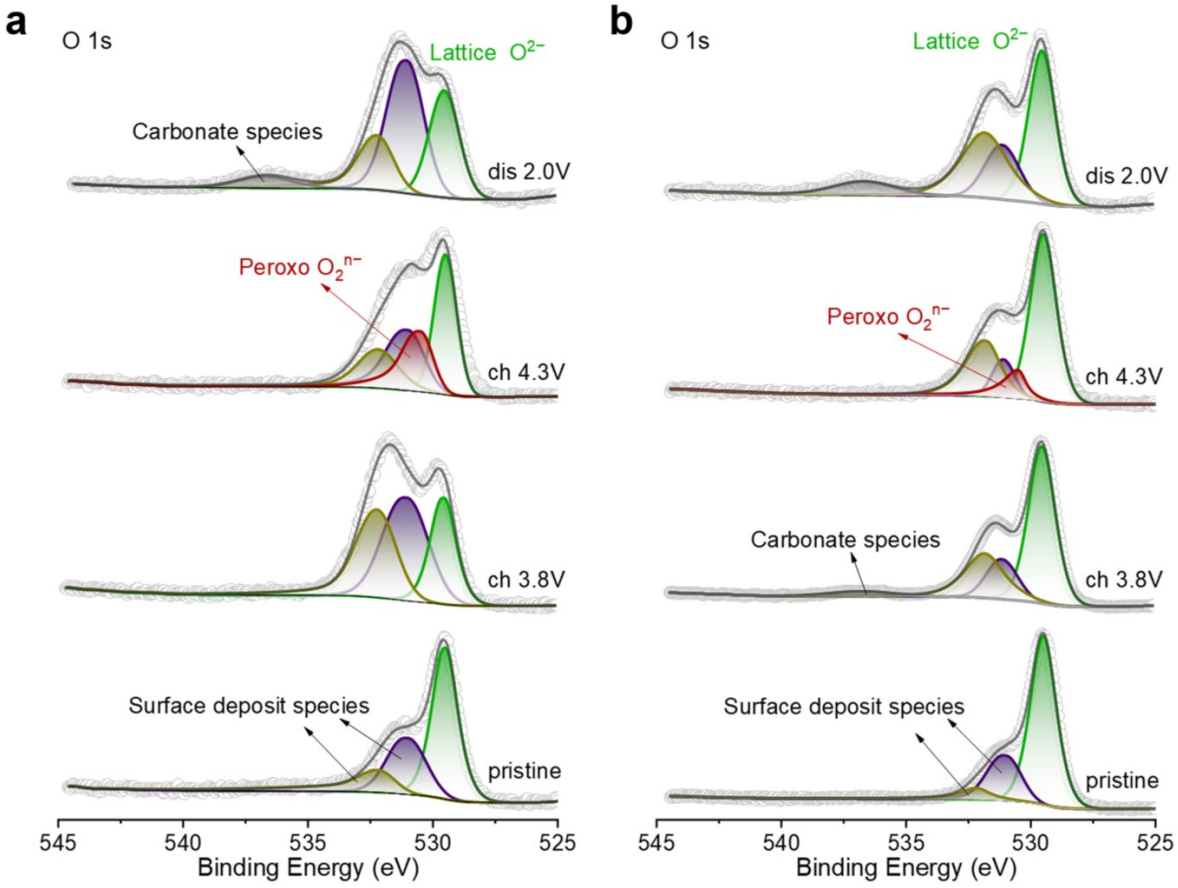

Fig. S20. O 1s XPS analysis of (a) NLRMO and (b) NLMO during the initial cycle.

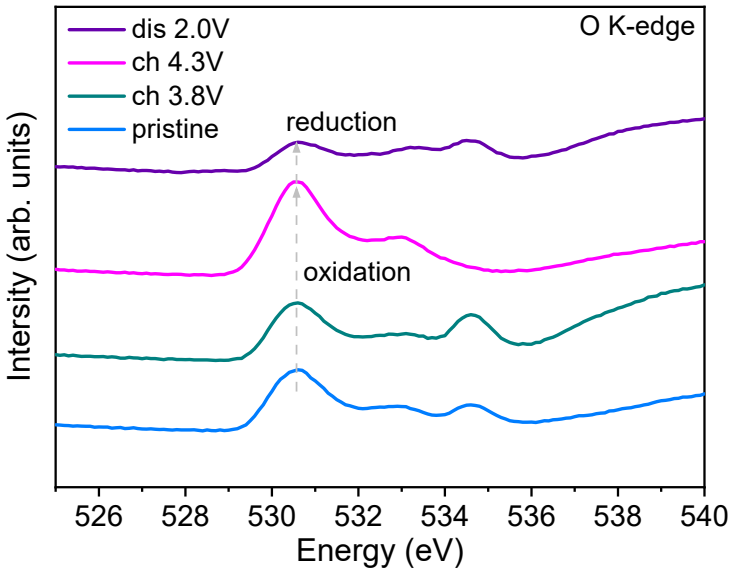

Fig. S21. O K-edge XANES spectra of NLMO during the initial cycle.

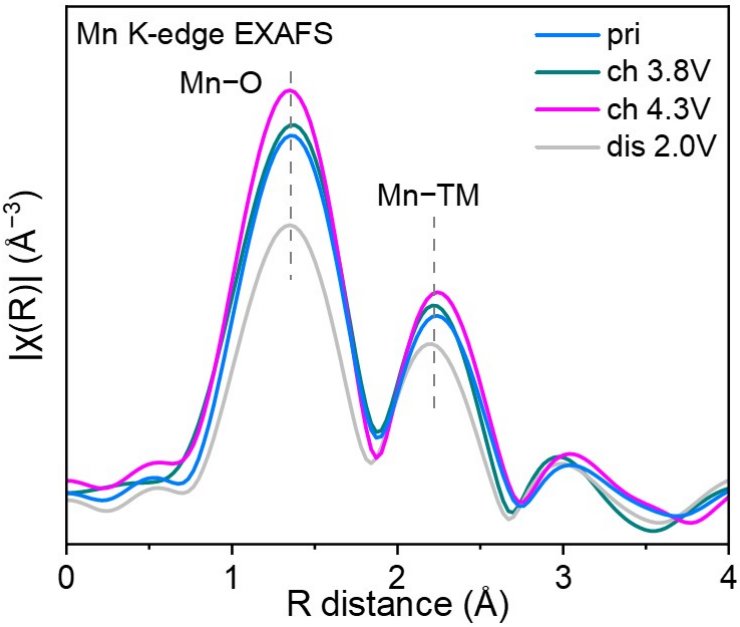

Fig. S22. FT-EXAFS spectra of Mn K-edge for NLRMO during the initial cycle.

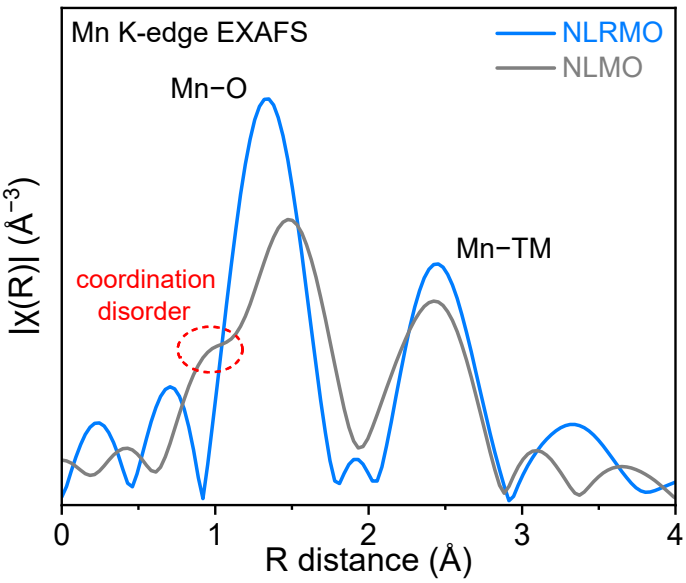

Fig. S23. FT-EXAFS spectra of Mn K-edge for NLRMO and NLMO after 40 cycles.

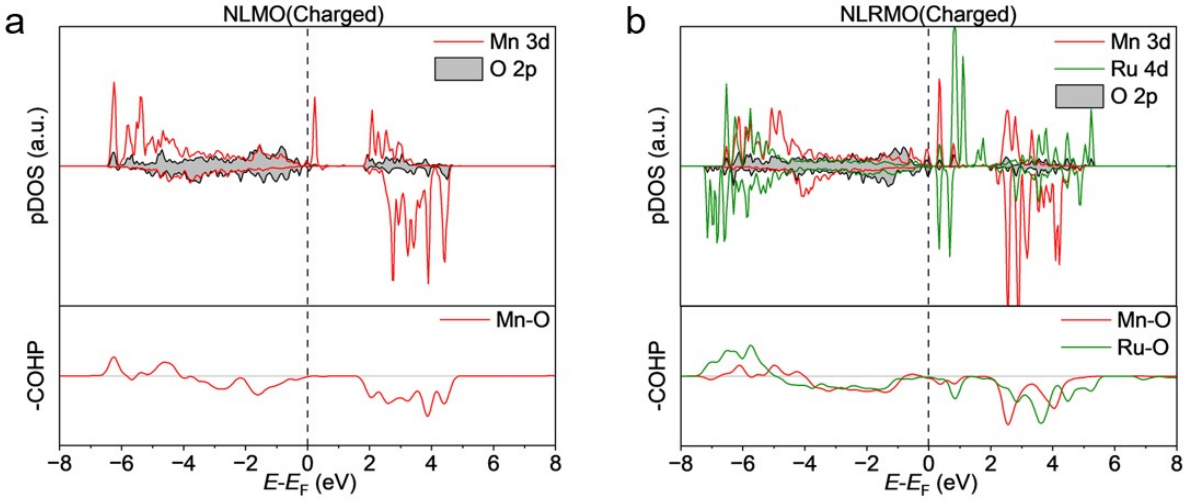

Fig. S24. Calculated electronic structure for (a) NLMO and (b) NLRMO in charged state.

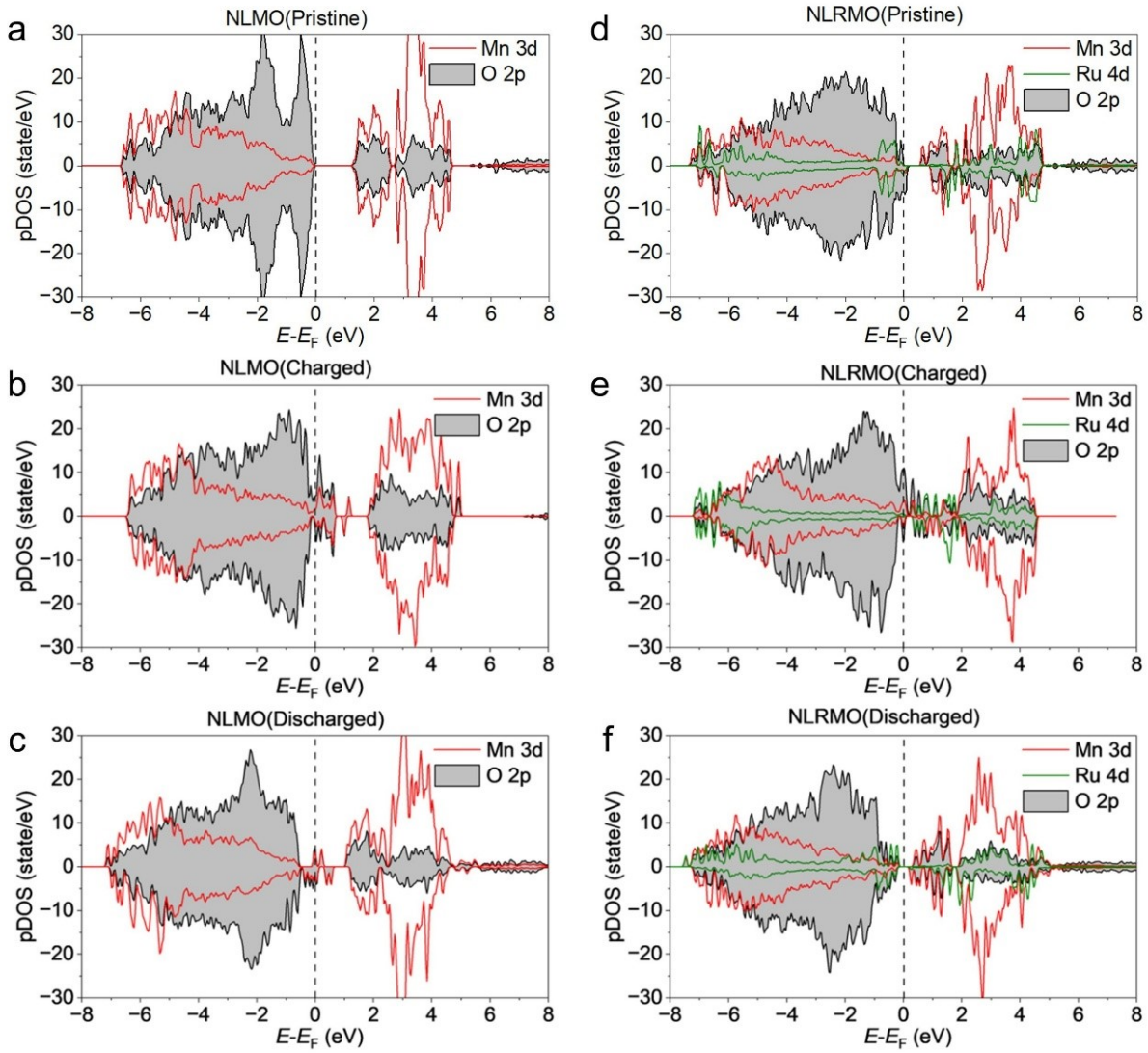

Fig. S25**.** Total DOS for (a, b, c) NLMO and (d, e, f) NLRMO in pristine, charged, and discharged state.

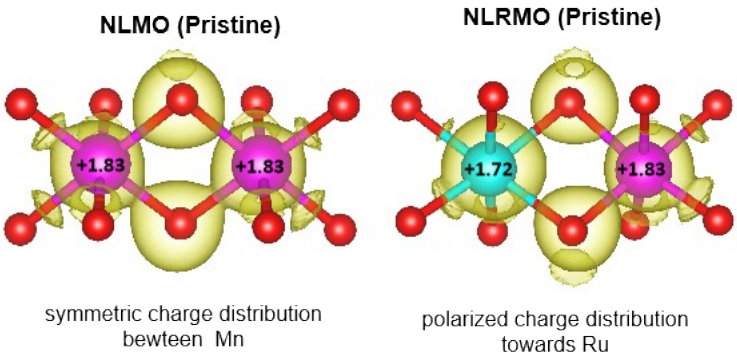

Fig. S26**.** The isosurface of electron density for NLMO and NLRMO in pristine state.

Supplementary Tables

Table S1. Refined crystallographic parameters of NLRMO by Rietveld analysis. a = b = 5.00385 Å, c = 11.07994 Å. α = β =90°, γ = 120°. V = 240.257 Å^3 . R*wp* = 7.77 %, χ^2 = 1.42. Space group: *P6$_3$*.

Atom	Site	*x*	*y*	*z*	Occ.
Na_f1	2a	0	0	1/4	0.1
Na_f2	2b	1/3	2/3	1/4	0.12
Na_f3	2b	2/3	1/3	1/4	0.12
Na_e	6c	1/3	0	1/4	0.34
Li1	2a	0	0	0	0.09
Li2	2b	1/3	2/3	0	0.02
Li3	2b	2/3	1/3	0	0.41
Ru1	2a	0	0	0	0.01
Ru2	2b	1/3	2/3	0	0.46
Ru3	2b	2/3	1/3	0	0.09
Mn1	2a	0	0	0	0.9
Mn2	2b	1/3	2/3	0	0.52
Mn3	2b	2/3	1/3	0	0.5
O1	6c	0.017	0.66423	0.1172	1
O2	6c	0.33992	0.98867	0.90881	1

Table S2. Refined crystallographic parameters of NLMO by Rietveld analysis. a = b = 2.86039 Å, c = 11.03103 Å. α = β =90°, γ = 120°. V = 78.162 Å^3 . R*wp* = 5.54 %, χ^2 = 1.14. Space group: *P6$_3$/mmc*.

Atom	Site	*x*	*y*	*z*	Occ.
Na1	2b	0	0	1/4	0.25
Na2	2d	2/3	1/3	1/4	0.44
Li	2a	0	0	0	0.23
Mn	2a	0	0	0	0.77
O	4f	2/3	1/3	0.10078	1

Table S3. Detailed information on the materials referenced in **Fig. 2g**. The conversion between the rate and current density is as follows: 1 C = 100 mA g^{-1}.

No.	Chemical Formula	Rate (C)	Cycle Numbe	Capacity Retention	Voltage Range	Ref.
1	P2-$Na_{0.76}Ca_{0.05}Ni_{0.23}Mn_{0.69}O_2$	0.12	50	87.1%	**2-4.3 V**	*Adv. Funct. Mater.* **31**, 2106923 (2021)
2	P2-$Na_{0.83}Mg_{0.33}Fe_{0.17}Mn_{0.5}O_2$	0.5	100	85.6%	**2-4.2 V**	*Adv. Energy Mater.* **13**, 2300746 (2023)
3	P2-$Na_{0.67}Li_{0.1}Fe_{0.37}Mn_{0.53}O_2$	2	100	84.5%	**2-4.3 V**	*Nat. Energy* **9**, 184-196 (2024)
4	P2-$Na_{7/9}Li_{1/9}Ni_{2/9}Mn_{5/9}Ti_{1/9}O_2$	1.5	200	90.2%	**2-4.3 V**	*Nano Energy* **100**, 107482 (2022)
5	O3-$NaLi_{1/9}Ni_{2/9}Fe_{2/9}Mn_{4/9}O_2$	2.5	200	82.8%	**2-4.3 V**	*Nat. Commun.* **12**, 5267 (2021)
6	P2-$Na_{0.63}K_{0.03}Ni_{0.26}Zn_{0.07}Mn_{0.67}O_2$	5	200	81.2%	**2-4.3 V**	*J. Energy Storage* **77**, 109933 (2024)
7	P2-$Na_{0.75}Ca_{0.04}[Li_{0.1}Ni_{0.2}Mn_{0.67}]O_2$	10.7	300	93.2%	**2-4.3 V**	*Adv. Funct. Mater.* **32**, 2203424 (2022).
8	P2-$Na_{0.85}Li_{0.12}Ni_{0.198}Be_{0.011}Mg_{0.011}Mn_{0.66}O_2$	5	300	78.3%	**2-4.3 V**	*Sustainable Energy Fuels* **8**, 1304-1313 (2024)
9	P2-$Na_{0.65}Li_{0.08}Cu_{0.08}Fe_{0.24}Mn_{0.6}O_2$	2	500	88.2%	**2.5-4.2 V**	*Nano Energy* **88**, 106206 (2021)
10	P2-$Na_{0.62}Mn0.67Ni_{0.23}Cu_{0.05}Mg_{0.07}Ti_{0.01}O_2$	1.2	500	87%	**2-4.3 V**	*Nat. Commun.* **13**, 2826 (2022)
11	P2-$Na_{0.85}Li_{0.12}Ni_{0.22}Mn_{0.66}O_2$	11	500	85.4%	**2-4.3 V**	*Angew. Chem. Int. Ed.* **59**, 14511-14516 (2020)
12	P2-$Na_{0.67}Ni_{0.2}Cu_{0.1}Co_{0.1}Mn_{0.6}O_2$	10	500	82%	**2-4.3 V**	*Energy Storage Mater.* **41**, 581-587 (2021)

Table S4. ICOHP Analysis.

Structure	-ICOHP	Structure	-ICOHP	
	Mn-O		Mn-O	Ru-O
Na18Li6Mn18O48	1.76856	Na18Li6Ru4Mn14O48	1.09748	2.77709
Na2Li6Mn18O48	1.73196	Na2Li6Ru4Mn14O48	1.48996	2.55555
Na14Li6Mn18O44	2.13421	Na14Li6Ru4Mn14O44	1.82016	2.49521

Table S5. Bader Charge Analysis.

Structure	Valance					Structure	Valance				
	Na	Li	Mn	Ru	O		Na	Li	Mn	Ru	O
Na18Li6Mn18O48	0.853	0.882	1.832	-	-1.117	Na18Li6Ru4Mn14O48	0.859	0.887	1.822	1.635	-1.100
Na2Li6Mn18O48	0.901	0.887	1.852	-	-0.843	Na2Li6Ru4Mn14O48	0.899	0.894	1.847	2.045	-0.858
Na14Li6Mn18O44	0.866	0.880	1.763	-	-1.117	Na14Li6Ru4Mn14O44	0.869	0.881	1.770	1.644	-1.109

Reference

1. Abdullahi YZ. Electronic and magnetic properties of RuO_2 monolayer: DFT+U investigation. *Comput Condens Matter* **29**, e00614 (2021).
2. Sun C*, et al.* A formation mechanism of oxygen vacancies in a MnO_2 monolayer: a DFT + U study. *Phys Chem Chem Phys* **13**, 11325-11328 (2011).